Structures of Silica-Based Nanoporous Materials Revealed by Microscopy

Lu Han,[a] Tetsu Ohsuna,[b] Zheng Liu,[c] Viveka Alfredsson,[d] Tomas Kjellman,[d] Shunsuke Asahina,[e] Mitsuo Suga,[e] Yanhang Ma,[f] Peter Oleynikov,[f] Keiichi Miyasaka,[g] Alvaro Mayoral,[h] Isabel Díaz,[i] Yasuhiro Sakamoto,[j] Sam M. Stevens,[k] Michael W. Anderson,[l] Changhong Xiao,[f] Nobuhisa Fujita,[m] Alfonso Garcia-Bennett,[f] Kyung Byung Yoon,[n] Shunai Che,[a] and Osamu Terasaki*[f,g]

Abstract. Ordered nanoporous structures are among the most fascinating and industrially important materials currently in use. The archetypal zeolite material has now been joined by an eclectic array of new structures that exhibit porosity over a wide range of length scales and with order/disorder expressed in a multitude of ways. This raises the bar in terms of characterization and extends a real challenge to the scientific community to fully understand the properties and potential future applications of such materials. In this review we discuss the importance of modern microscopy tools combined with diffraction in this endeavour and show how the details of even the most complex quasi-crystalline nanoporous architectures can be elucidated. We show by using the appropriate spherical aberration (C_s) corrections in scanning transmission electron microscopy it is possible to decipher all the individual silicon and aluminum atoms in a zeolite structure. Automated routines for using large electron diffraction datasets for crystal structure determination of nanocrystals is described making the need for large single crystal synthesis less-and-less important. The power of complementary combinations of surface tools such as atomic force microscopy and high-resolution scanning electron microscopy is discussed to elucidate crystal growth mechanisms. For mesoporous materials synthesized from self-organized organic mesophases electron microscopy reveals the details of the complex hierarchy of porosity so crucial for the functional performance of the structure.

Special Issue

* Prof. Dr. O. Terasaki
  Fax: +46-8-152187
  E-Mail: terasaki@mmk.su.se; terasaki@kaist.ac.kr
[a] School of Chemistry & Chemical Engineering
  Shanghai Jiao Tong University
  Shanghai, P R China
[b] Kagami Memorial Laboratory for Materials Science and Technology
  Waseda University
  Tokyo 169–0051, Japan
[c] Nanotube Research Center
  National Institute of Advanced Industrial Science and Technology (AIST)
  Tsukuba 305–8565, Japan
[d] Physical Chemistry
  Lund University, Sweden
[e] JEOL Ltd. SM BUSINESS UNIT
  Tokyo, Japan
[f] Department of Materials & Environmental Chemistry, EXSELENT
  Stockholm University
  Stockholm, Sweden
[g] Graduate School of EEWS, KAIST
  Daejeon, Republic of Korea

[h] Laboratorio de Microscopias Avanzadas
  Nanosience Institute of Aragon
  Universidad de Zaragoza, Mariano Esquillor, Edificio I+D
  Zaragoza, Spain
[i] Instituto de Catalisis y Petroleoquimica CSIC
  Madrid, Spain
[j] Nanoscience and Nanotechnology Research Center
  Osaka Prefecture University
  Sakai 599–8570, Japan
[k] Private Contributor
  UK
[l] Centre for Nanoporous Materials
  School of Chemistry University of Manchester
  Manchester, UK
[m] Institute of Multidisciplinary Research for Advanced Materials
  Tohoku University
  Sendai 980–8577 Japan
[n] Department of Chemistry
  Sogang University
  Sinsu-Dong, Mapo-Gu
  Seoul 121–742, Korea

(I) Introduction

Ordered porous materials exhibit a great diversity of novel properties depending on their particular structural parameters. They are classified into micro- (< 2 nm), meso- (2–50 nm) and macro-porous (> 50 nm) solids according to the size of the pore diameter and arrangement (or gas adsorption behavior). Herein we focus on the porous materials with the pore size in nanometer range, mainly include microporous zeolite crystals and mesoprous silicas. Their characteristic features are strongly dependent on the surfaces, crystal boundaries, and defects. In order to characterize these aspects as well as to understand the formation mechanism of these materials, electron microscopy (EM) and atomic force microscopy (AFM) can provide unique and direct information of both projected structure and surface fine structure.

We begin this review with the minimum necessary information regarding EM for a structural study on silica nanoporous crystals and then give specific examples.

Transmission electron microscopy (TEM), scanning electron microscopy (SEM), and scanning transmission electron microscopy (STEM) are commonly used EM techniques. Utilising an electron source with high brightness and coherence is essential for EM. There are two extreme modes of electron beam illumination of a sample: one is parallel (i.e. plane wave) illumination, in order to obtain sharp electron-diffraction (ED) patterns or high-resolution TEM (HRTEM) images; the other is convergent illumination onto a very small area of the sample for convergent beam ED (CBED). A convergent-beam can be used for imaging by raster scan over the crystal surface using a scanning coil in order to perform STEM and SEM observations. Accelerating voltages lie in the range of 15–1250 kV for TEM and STEM, and 1–30 kV for SEM. Notably, electron lenses are poorly inherent compared to optical lenses and the resolution of TEM is limited by spherical aberration (C_s), whereby high-angle beams (near the edge) have a premature focus and cause image distortion. With a corrector (quadrupole-octupole corrector or the hexapole corrector) that produces negative C_s to give a total $C_s \approx 0$, the resolution of TEM can be greatly enhanced.[1]

For structural characterization of nanoporous silica crystals the advantages of EM approaches over X-ray diffraction are: (i) average periodical structure solutions can be obtained even from nanometer-sized crystals from a set of ED patterns; (ii) structural deviations from perfect periodicity, including fine structures of surface, interfaces, boundaries, and structural modulations, can be observed locally via the images; (iii) the chemical and elemental characterizations of the sample can be obtained by spectroscopy such as energy-dispersive X-ray spectroscopy (EDS) and electron energy loss spectroscopy (EELS); (iv) furthermore, point-by-point mapping information can be obtained through scanning with convergent beam. By using STEM, annular dark-field imaging (ADF) and high-angle annular dark-field imaging (HAADF) can be observed. As the image contrast of HAADF is proportional to Z^n (Z: atomic number, $n \approx 2$) and the image is not affected by the contrast transfer function (CTF), it is possible to form atomic-resolution images. Also, as the heavy atoms can be highlighted, dis-

tributions of metal atoms as catalysts loaded in the mesoporous solids can be revealed with HAADF and tomography. It has been shown that the EDS, EELS, and tomography are capable of locating templates and organic molecules within the pores of the mesoporous materials.[2,3] For zeolites, the elemental analysis by EDS and EELS is more macroscopic due to the beam damage and the information of the guest elements needs to be extracted by image analysis, which is facilitated by the difference in Z.[4] Figure 1 schematically represents the main processes considered in this review for situation (ii). Some of the recent works on situation (i) are also reviewed briefly.
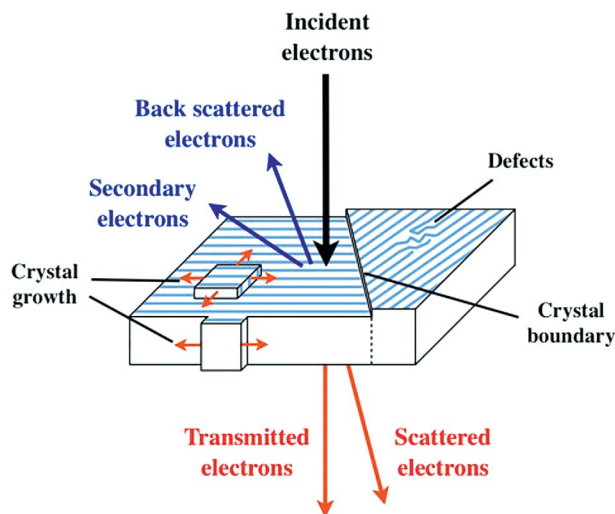

Figure 1. Schematic drawing for the signals generated using high-energy electron beam and a thin specimen.

TEM and STEM give projected structural information, while SEM and AFM give surface-selective information. The superiority of the SEM and AFM with respect to the optical microscope is, in particular, the high spatial resolution, large depth of field (SEM) and the very high resolution in height (AFM). By combining AFM and SEM we can observe surface-topological information from a large specimen area with large height difference at high resolution.

(II) TEM and STEM

Many nanoporous materials are electrical insulators and are very sensitive to electron beam radiation. Different types of beam damage, i.e. ionization, displacement, reduction, structure collapse, can be observed depending on the type of the materials and the bonding nature. To overcome the electron-beam-damage problem, the accelerating voltage should be not too high; the beam density during the observations should be as low as possible and the CCD camera needs to be very sensitive to minimize the total dose received by the specimen to levels below the damage threshold. Even so, a long exposure time is expected and sometimes the sample drift becomes a big issue. Notably, a single HRTEM image with a long exposure time can be substituted by a sequence of frames recorded with short exposure time and superimposed after drift compensation.

For the case of STEM, the convergent electron beam has a higher beam density that is even increased (under normal working conditions) with the implementation of the C_s correctors; therefore the materials are damaged even faster than using parallel beam. Luckily, by minimizing the beam current and using fast scanning times,[5,6] C_s-corrected STEM has provided unprecedented resolution images is a possible solution as only the part of the crystal observed at high-magnification, while the rest remains intact.

Also, the environmental transmission electron microscope (ETEM) with the ability to image the sample in a controlled gaseous environment has been developed for observation the reaction processes such as crystal nucleation and growth, heterogeneous catalysis and so on.

(A) Zeolites

Zeolites are crystalline microporous materials and have been widely used as heterogeneous catalysts. Zeolites are commonly synthesized by a hydrothermal method combining silica and alumina sources. The frameworks are built from corner-sharing TO_4 tetrahedra (T = Si, Al, P, Ga, Ge, etc.) connected by oxygen bridges that produce channels or cavities of molecular dimensions.

(A-1) Average Structures

Average structures of zeolites are often obtained using electron microscopy through ED patterns and HRTEM images.

(a) By Electron Diffraction

Dorset and *Hauptman*[7] were the first to apply the direct method for ED intensity data obtained from organic macromolecules, and they gave the phases of reflections through the phase correlations based on the fact that the scattering density must be a positive real number. Dorset showed the power of electron crystallography (EC) for various crystals. *Carlsson* et al.[8] obtained a framework structure and localized the iron atomic position of Fe-oxide incorporated in a cavity of Na-Y (FAU). *Dorset* and *Gilmore*[9] further refined the crystal structure of Na-Y from 87 unique reflections observed by *Carlsson* et al., using a maximum-entropy and -likelihood approach. *Wagner* et al.[10] solved the unknown structure of a large-pore, high-silica zeolite, SSZ-48, from a set of ED data (326 unique reflections) by the direct method.

The main drawback of the conventional approaches for collecting a set of ED patterns is the low performance in comparison to automated X-ray diffraction. The precession ED method with conical electron beam precession,[11] which has gained popularity among the EC community, is often used today for collection of high quality and less-dynamical ED intensity data.[12,13] However, this method can cover a rather limited part of reciprocal space. The real three dimensional (3D) ED data can only be recorded using other methods such as electron diffraction tomography.[14–16] The first method combines crystal tilting (usually with 1° steps around the principal sample holder axis) followed by acquisition of a hardware precession electron diffraction pattern (known as automated diffraction tomography, ADT[14,15]). The second method is similar, however, it utilizes a software-induced electron beam tilt (typically 0.1° beam-tilt steps) along a line instead of a hardware conical precession (known as 3D electron diffraction tomography, 3D-EDT[16]). The ADT data collection experiment produces ca. 100 individual precession frames, while the EDT method has much higher throughput resulting in 800–2000 individual electron diffraction patterns taking similar or shorter times compared with ADT. In addition, the EDT method has much finer reciprocal space sampling that allows quantification of diffuse scattering and analysis of reciprocal shape of reflections (rocking curves) in 3D.

The main advantages of both methods are: (i) the crystal does not need to be oriented during the whole data collection and (ii) reduced dynamical scattering effects on ED intensities. Some parts of reciprocal space cannot be scanned because of the limitation of the sample holder (20–55 % of total reciprocal space depending on the holder used). In this case, crystals with low symmetry such as triclinic and monoclinic crystal systems will have lower data completeness.

Both ADT and EDT methods are very powerful for phase analysis, which can be a very complicated task in the case of powder X-ray diffraction (PXRD). For the purpose of the 3D unit cell determination the scanning steps can be 1° in both methods and the total reciprocal space scan can be done only for 30–50°, which significantly speeds up the data collection. An example of how 3D EDT was used for unit cell determination can be found for the most complex intergrowth zeolite ITQ-39.[17] In order to solve the structure of ITQ-39 a combination of PXRD, HRTEM imaging and 3D EDT was used. In this review we briefly show our recent study of ETS-10.

Irrespective of the data collection methods, high quality data can be used for further determination of 3D crystal structures of zeolites and other porous materials.[18–20]

(b) By TEM & STEM Images

Ohsuna et al.[21] solved uniquely the structure of zeolite BEC through analysis of HRTEM images with the help of a Patterson pair map obtained from the ED patterns. By a combination of high-resolution powder XRD and HRTEM images, *McCusker* et al. also solved diverse and very complicated zeolites structures.[22,23]

It is difficult to observe individual T (Si, Al) atoms even using a high-voltage, high-resolution TEM (HVHRTEM, JEM-1250 taken at 1250 kV, Tohoku University, which was unfortunately broken by the Tohoku earthquake on 2011.03.11) with spatial resolution close to 1 Å. However, nowadays it is possible to observe individual atomic columns through C_s-corrected STEM.[5,24] In this respect it is useful and informative to compare HVHRTEM images and C_s-corrected STEM-HAADF images of Na-LTA and MFI (Figure 2).

Bright dots in an HRTEM image correspond to pores, while they correspond to atomic positions in an STEM-HAADF image. The dark contrast observed at the center of an *a*-cage in
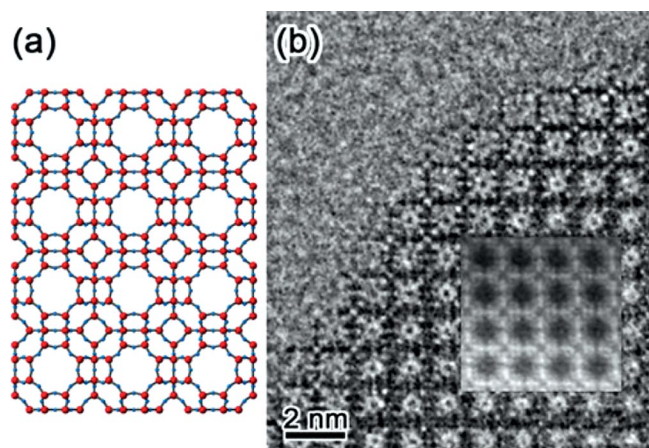
Figure 2. Framework structure of LTA zeolite with <100> incidence (a), the HVHRTEM image taken at 1250 kV by JEM-1250 with <100> incidence and the STEM-HAADF image taken by XFEG FEI Titan (operating at 300 kV, convergence semiangle = 24.8 mrad, and collection angle = 70 to 200) is inserted (b). STEM-HAADF image is taken from reference[5].
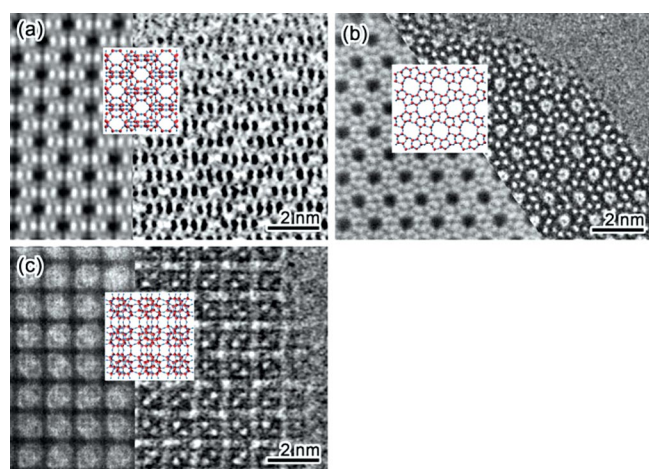

Figure 3. Comparison of HVHRTEM taken at 1250 kV by JEM-1250 (right) and STEM-HAADF taken by by XFEG FEI Titan (operating at 300 kV, convergence semiangle = 24.8 mrad, and collection angle = 70 to 200) (left) images of MFI for [100] (a), [010] (b) and [001] (c) directions. Frameworks of the projections are also inserted. HRTEM image of [100] is taken from reference[27] and STEM-HAADF images are from reference[24].

TEM images is due to an artefact induced from electron-optical effects. This is discussed in detail by *Alfredsson* et al.[25,26] and the same effect is observed in the following HRTEM images. Amazingly all Si and Al positions are observed in STEM-HAADF. It is, however, to be noted that we can characterize structures of silica nanoporous crystals in most cases even from the pore geometry, i.e., a size/shape and pore arrangement (and therefore symmetry), which are the most important structural features in porous materials. This is clearly shown in the following work on the MFI structure with space group symmetry *Pnma* (*a* = 20.09 Å, *b* = 19.74 Å, *c* = 13.14 Å) (Figure 3).

(A-2) Structure Modulations: Fine Structures of Boundaries, Surface Termination, and Defects

There are many interfaces and boundaries, and among them the surface is the most important as reactant molecules enter the crystals through the surface. Surface fine structure also gives information concerning the crystal growth process. After solving the structure of zeolite BEC by *Ohsuna* et al.,[21] a new structure type C of zeolite beta was found. There was a report of a germanate with the same framework topology of BEC,[28] however, it is well known that the chemistry of germanates and silicates are quite different. Figure 4 shows an HRTEM image of BEC taken with [100] incidence and simulated images for different structure terminations are inserted. Two different surface terminations, double four-membered ring (D4R) and D4R free, are observed on both (010) indicated by red and blue arrows, respectively, and (001) indicated by green and black arrows, respectively.[29] Energetic discussions of these corresponding surface terminations has been reported by *Slater* et al.,[30,31] suggesting that two-step S4R addition (quickly reacts to give the D4R) and one-step D4R addition may happen.
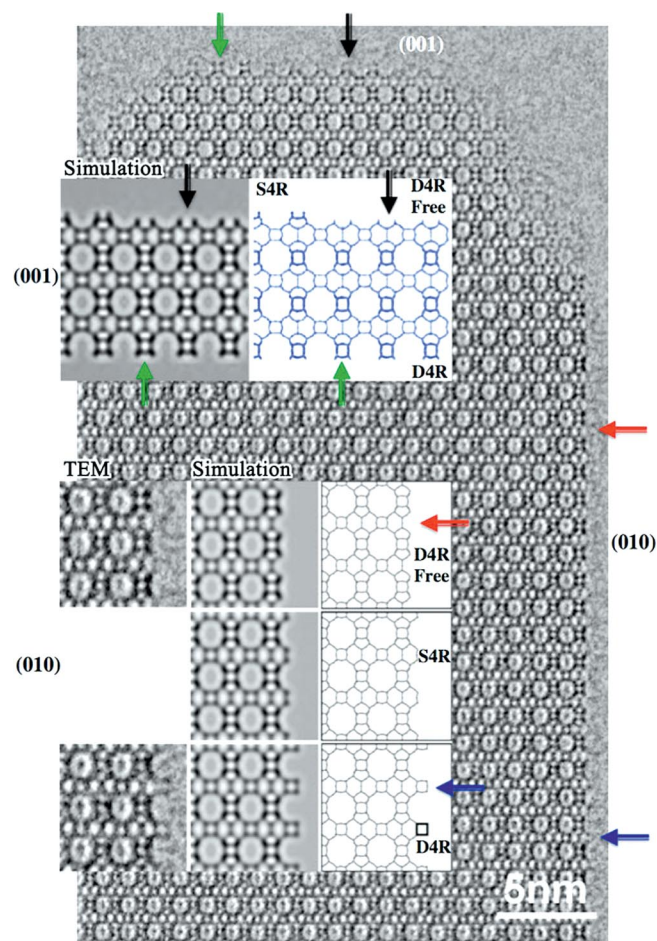

Figure 4. HRTEM image of zeolite BEC taken with [100] incidence at 400 kV by JEM-4000EX.[29] The surface termination indicated by arrows from two different surfaces of (001) and (010) are enlarged with the corresponding HRTEM simulation and the structural models.

Figure 5 shows another example of the HRTEM images of faujasite (FAU) and EMT zeolites. Structures of both EMT and FAU zeolites are formed from the same layer structure called the "FAU sheet" and successive sheets are stacked with mirror or inversion, respectively, as shown schematically in Figure 5a,b. Figure 5c shows clearly the manner of the intergrowths of FAU and EMT from highly crystalline samples. Figure 5d shows both surface terminations at {111} surface without double 6-rings (D6Rs) and a twin plane of FAU. It is obvious from the image that the EMT framework is formed locally at the twin plane. It is rare to observe the framework so clearly at the boundaries that the framework of the twin plane is well connected.[32]
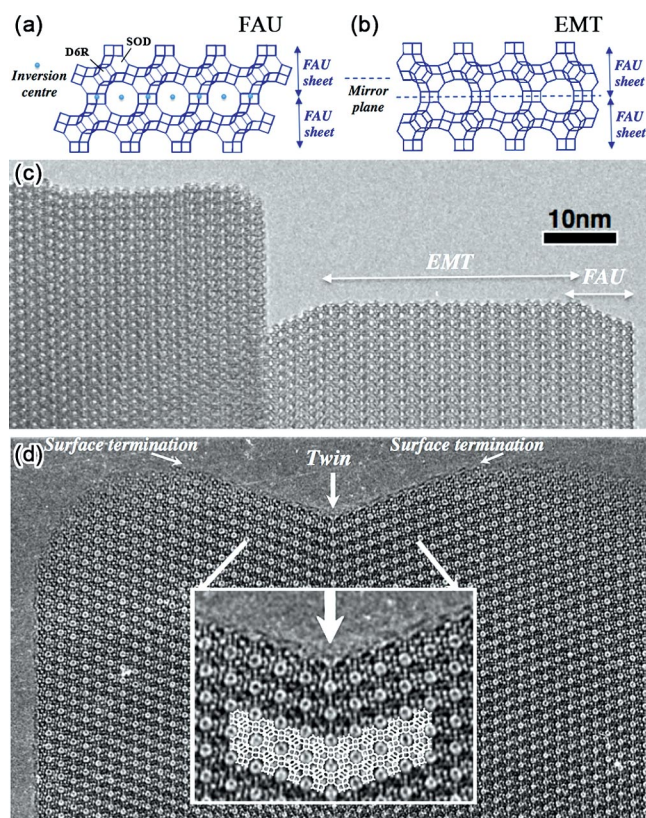

Figure 5. HRTEM image of FAU and EMT zeolites taken with JEM-4000EX at 400 kV. Structures of FAU and EMT lattices, which are composite of FAU sheets by inversion and mirror symmetries, respectively. Si atoms correspond to vertices, D6Rs, sodalite (SOD) cages, and FAU sheets are indicated.[32]

Titanosilicate ETS-10 [$Ti_{16}Si_{80}O_{208}(Na, K)_n$] is an electron beam stable nanoporous crystal compared to zeolites with high Al concentration. SEM images of ETS-10, HRTEM image, and corresponding selected area ED (SAED) pattern, and 3D-EDT pattern are shown in Figure 6. Using the SEM image plus the ED patterns and HRTEM images, it was confirmed that ETS-10 has fourfold symmetry in projection along the z axis and that the projected structures along x and y axes are identical. The key basic structural unit was determined to be an –O–Ti–O–Ti–O– chain constructed from corner-sharing TiO_6 octahe-

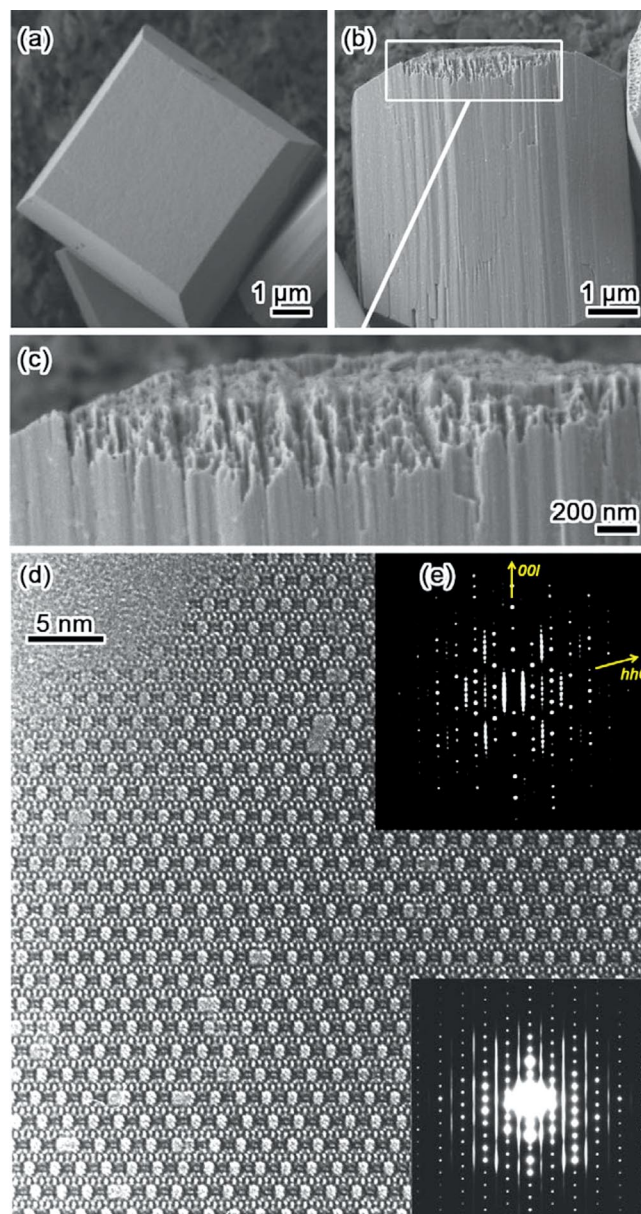dra surrounded by Si–O linkages, and its connectivity was derived by EM observations (Figure 7).

Figure 6. Top view SEM image of ETS-10 taken by JEOL JSM-7401F with the accelerating voltage of 1 kV (a); side view from another crystal (b) and (c);[35] HRTEM image taken at 400 kV by JEM-4000 from [110] of polymorph B and [100] of polymorph A with the corresponding SAED pattern (d);[38] the 3D EDT data of the crystal (e).[35]

The 3D ED intensity data set, 1530 frames in total collected by tilting from –62.7° to +68.9° (132° in total) with step 0.15°, was collected by the 3D EDT method using a JEOL 2100 LaB_6 and Gatan Erlangshen CCD camera. Possible unit cell parameters were determined to be $a = b = 21$ Å, $c = 14.5$ Å, $\alpha = 90°$, $\beta = 111.12°$, and $\gamma = 90°$, with space group $C2/c$ (this corresponds to the polymorph B, which is discussed later). Twins with common c^* axis and mirror planes parallel to [1–10] direction were also observed. Assuming 50% mixture of twins
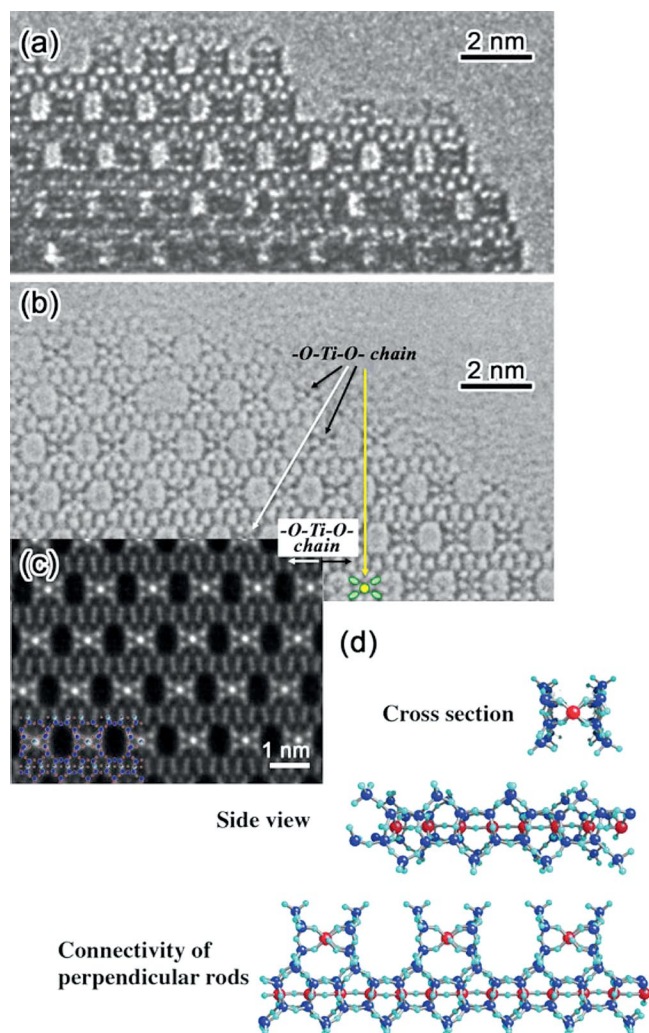
Figure 7. HRTEM images taken with JEM4000 at 400 kV (a) and JEM-1250 at 1250 kV (b); STEM image taken by by XFEG FEI Titan (operating at 300 kV, convergence semiangle = 17 mrad and collection angle 50 to 200 mrad) (c) and the schematic drawing of the two extreme cases of stacking of the rods, polymorph A and B (d).[6,38]

Figure 8. Schematic drawing of the two extreme cases of stacking of the rods, polymorph A and B.

(B) Silica Mesoporous Crystals

The synthesis and structural analyses of mesoporous silica are of great interest because of their potential for new applications in adsorption, catalysis, sensor design, drug delivery, and nanotechnology.[39–41] Although the silica matrix of mesoporous materials is amorphous, the mesopores are arranged periodically, forming an ordered network with a well-defined crystallographic symmetry. Thus, the mesoporous silica can be considered as "cavity crystals" and called silica mesoporous crystals (SMCs).

(B-1) Average Structure Solutions of SMCs

In order to obtain a structure solution for SMCs it was necessary to develop a new electron crystallography based on the facts that (i) the amorphous silica walls and pores are arranged periodically and show crystal morphology, which is commensurate with their point group symmetry, and (ii) it is hard to observe extinction conditions of SMCs from the selected area ED patterns because of dynamical scattering. For example, we could not observe proper extinction conditions from MCM-48 crystal for obtaining space group $Ia\bar{3}d$. So our approach was to take HRTEM images from different zone axes and to obtain crystal structure factors from very thin area in the images, both amplitudes and phases, through Fourier diffractograms. Subsequently it is possible to reconstruct 3D-electrostatic potential maps uniquely based on the space group symmetry.[42–44] So far, we have solved various structures by electron cyrstallography reconstruction methods and they are shown as a function of g-parameters together with P-surface & tricontinuous structures by *Wiesner* et al.[45] and *Han* et al.[46] (Figure 9).

It is worthy to note that the fine structure of the porous system, e.g. the pore geometry, the nature of the wall, defects and intergrowth, and the formation mechanism are very important. Compared to the traditional atomistic crystals, the intergrowth and defects of mesoporous silicas are more diverse due to the framework wall being flexible before completion of silica polymerization and the structures are sensitive to the synthesis conditions. In the following we discuss not only various types of defects but also the quasicrystalline state.

and using the charge flipping (an iterative algorithm for solving the phases from structure factor amplitudes) method,[33,34] we can obtain all atomic positions of Si, Ti, and O atoms except three oxygen positions from 3D-EDT data (Figure 6e) [35]. Figure 7a,b are HRTEM images taken at 400 kV by JEM-4000EX and 1250 kV with JEM-1250, respectively. Figure 7c corresponds to the C_s-corrected STEM image taken by the XFEG FEI Titan (University Zaragoza) with an aberration corrector for the electron probe recorded at 300 kV. An HRTEM image (Figure 7a) gives important information on the pore arrangement and the framework connectivity, and gives hints to build a primary structure unit (Figure 7d). The surface structure presented suggests that a rod is the secondary building unit being also the growth unit in ETS-10. The STEM image clearly shows all Ti and Si atomic positions[6] of the structure solved by *Anderson* et al.[36–38] Two extremes of the rod stacking, ideal structures of polymorphs A and B, were proposed from the observations as shown in Figure 8.
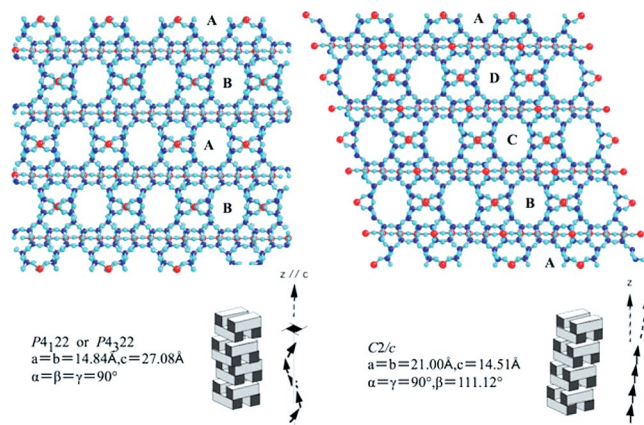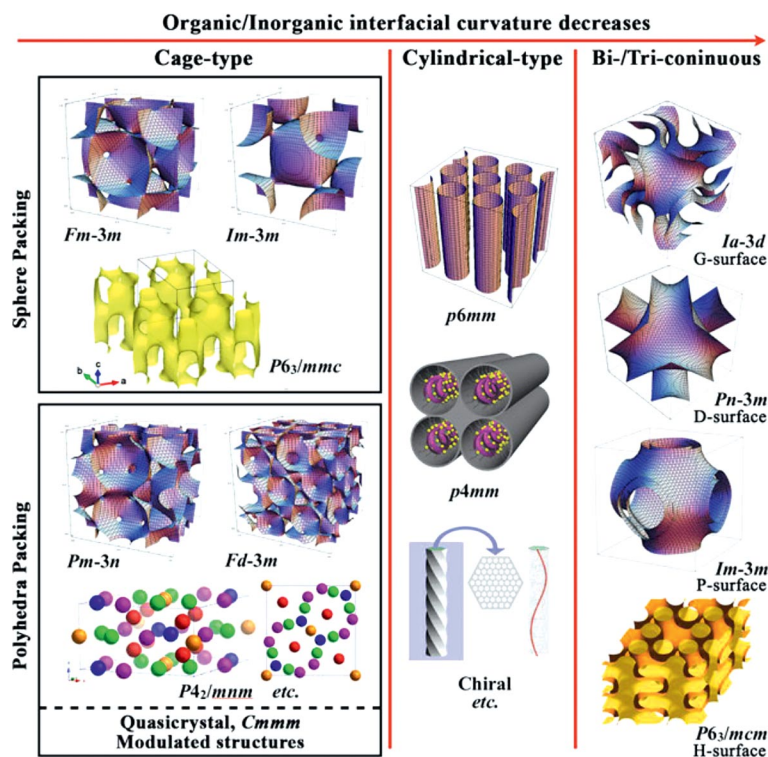
Figure 9. The structures of the SMCs. Cage-type structures (left), 2D cylindrical structures (middle), triply periodic minimal surfaces (right) and the bilayer structures (not shown) can be formed with decreasing the organic/inorganic interfacial curvature.

(B-2) Structure Modulations

(B-2-1) Defects in Bicontinuous Structures

MCM-48 is a complex 3D structure with space group symmetry $Ia\bar{3}d$ with point group (PG) symmetry $m\bar{3}m$, having a bicontinuous mesostructure divided by a Gyroid (G-) minimal surface. AMS-10 is another type of bicontinuous SMCs with a Diamond (D-) minimal surface (space group $Pn\bar{3}m$).[47]

Recently, a series of SMCs have been synthesized showing a systematic structural change of cage-type → 2D cylindrical $p6mm$ → epitaxial intergowth of $p6mm$ and D-surface → epitaxial intergowth of $p6mm$ and G-surface → D-surface → G-surface → lamellar in the mixture surfactant system.[48] The HRTEM image showed that the cylinders of $p6mm$ are parallel to the <110> of D-surface with a $\{11\}_{p6mm}\leftrightarrow\{221\}_D$ relationship, showing a "side-by-side" arrangement (Figure 10a,b), whereas for the G-surface two kinds of connection were found. It can be clearly observed from the HRTEM image that the cylinders of $p6mm$ are parallel to the <111> of G with both $\{10\}_{p6mm}\leftrightarrow\{211\}_G$ and $\{10\}_{p6mm}\leftrightarrow\{220\}_G$ relationship (Figure 10c,d). For the $\{10\}_{p6mm}\leftrightarrow\{220\}_G$ intergrowth, the cylinders of $p6mm$ domain cannot fit well the G domain perfectly, creating numerous defects with elliptical channels at the boundary (marked by the red arrows in Figure 10d. In another report, the structural transformation from 2D hexagonal $p6mm$ to G-surface, and to D-surface have also been achieved and an epitaxial relation has been observed between $[111]_G$ and $[110]_D$ orientations.[49]

Interestingly, the D-surface formed a unique spherical morphology with inner polyhedron hollows (icosahedral, decahedral, Wulff polyhedral, etc.) formed by the reverse multiply twinned D-surface structure (Figure 11).[50] Therefore, all of the domains are interconnected via a shared (111) surface and form an icosahedral shape, and the inner surface consists of twenty {111} facets. It has been found that vesicles with low-curvature lamellar structures were firstly obtained, then a structural transformation to D-surface structure occurred, which induced the formation of the reverse, multiply twinned icosahedral/decahedral hollows.

(B-2-2) Defects in Cage Type Structures, P6₃/mmc, Fm$\bar{3}$m, and Fd$\bar{3}$m

The cage-type mesostructures are formed by the packing of the spherical (also ellipsoidal) micelles with the highest organic/inorganic interfacial curvature. Up to now, different types of cage-type mesostructures have been synthesized, which provides us the opportunity to look into the structural relationships of these packing behaviors.

The closest packing of uniform spheres on a plane forms a layer with a hexagonal sphere arrangement, which will be called a "layer", the layer can be *A* or *B* or *C* depending on the origin of the spheres. The three-dimensional packing of these layers can be described by the stacking sequence of different layers, two special cases are the *ABCABC…* and *ABABAB…* stacking sequences. The point group symmetries of which are $m\bar{3}m$ and $\bar{6}m2$, respectively; therefore, the stackings
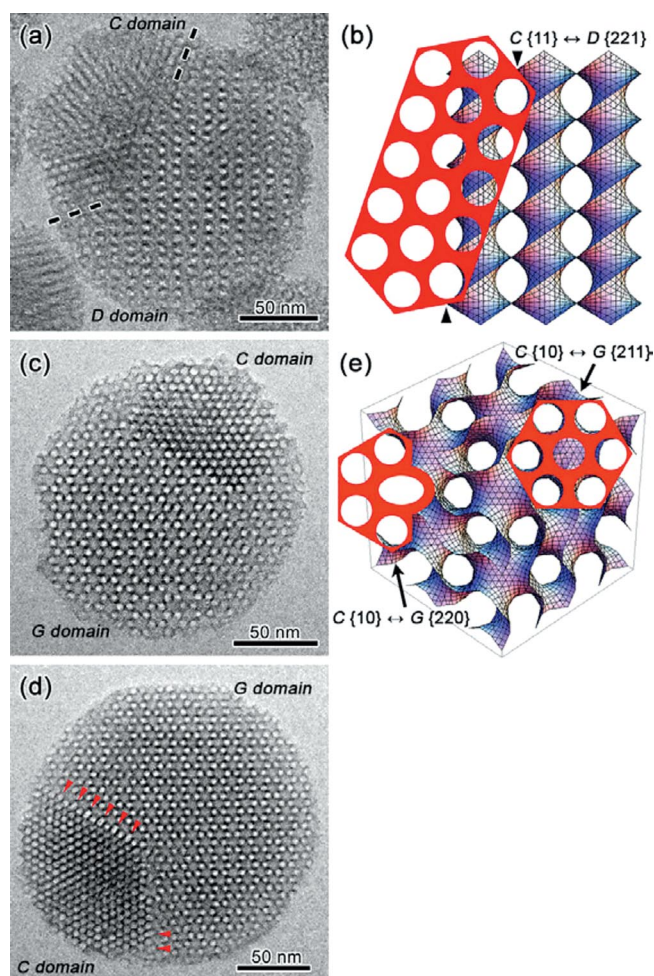
Figure 10. TEM images taken at 200 kV by JEM-2100 and the schematic drawing of the intergrowth of *p6mm* and D-surface structure taken along [110]$_{cubic}$ axis (a, b), intergrowth of *p6mm* and G-surface, taken along [111]$_{cubic}$ axis (c–e).[48]
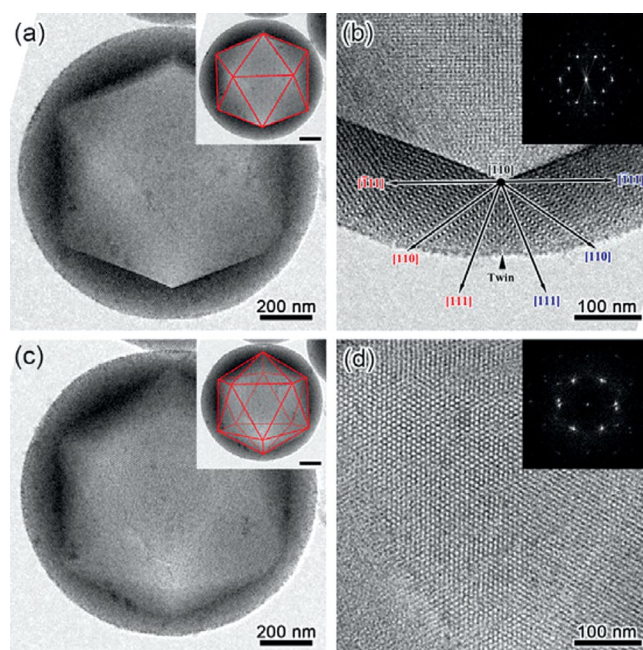

Figure 11. HRTEM images taken at 200 kV by JEM-2100 of an hollow SMC with an icosahedral hollow. (a) TEM image taken from the intersection edge of two triangles; the inset shows a structural model. (b) Magnified TEM image of the twin plane in (a). (c) TEM image taken from the center of a triangle, with a structural model shown in the inset. (d) Magnified TEM image of the center in (c).[50]

are called cubic close-packed (*ccp*) and hexagonal close-packed (*hcp*) structures, respectively. They are well-known as the structure having the highest packing density of perfect spheres of ca. 0.74 and are easily makes an intergrowth each other. The *ccp/hcp* structure produces two kinds of space at the interstices of the spheres. One is octahedrally surrounded by six spheres and the other is tetrahedrally surrounded by four spheres.

The intergrowth of *ccp/hcp* structures are often found in the SMCs as random packing of both structural domains sharing the [001] {or [001]$_{hex}$} and the [111]$_{cub}$ axis. Very recently, a pure *hcp* mesostructure with *P6$_3$/mmc* symmetry of SMCs has been obtained, which gives rise to hexagonal plate morphology (Figure 12a) and three-dimensional (3D) hexagonal structure (Figure 12b and c), although the *c/a* ratio of the crystal is close to 1.63 corresponding to an ideal sphere packing.[51] Furthermore, it has been revealed from the electron crystallographic 3D reconstruction that, small windows for connecting cages can be found not in *c* plane but only between layers along the *c* axis, which is different from the *ccp* SMCs (Figure 12d). As a result, the point group symmetry of mesopores becomes $\bar{6}m2$

instead of the $m\bar{3}m$ symmetry observed for perfect spheres in the *ccp*.

Notably, the existence of one *ABC* stacking layer can complicate the contrast of the HRTEM image along [0001] axes, as shown in Figure 13. The TEM images and averaged TEM image shows very different contrast from the image taken from [0001] of pure *hcp*. Panels d and e in Figure 13 show the structural model, where the *hcp* structure with *ABAB* stacking is changed to *BCBC* stacking by a *ccp* (*ABC*) layer and hence make very different projected image.

SBA-1 and SBA-6 (space group *Pm$\bar{3}$n*), AMS-8 (space group *Fd$\bar{3}$m*) and AMS-9 (space group *P4$_2$/mnm*) have multimodal cages, and the interstices of the spheres are only tetrahedrally surrounded. These structures are known as the *tcp* structures governed by area-minimizing effect rather than total packing entropy of *ccp/hcp* structure. In this case, the soft micelles make interfaces with the adjoint micelles and become polyhedra instead of the perfect spherical cages. Four types of polyhedra, 5^{12}, $5^{12}6^2$, $5^{12}6^3$, and $5^{12}6^4$, introduced for intermetallic compounds by *Frank* and *Kasper*, have been used for the construction of the *tcp* structures (Figure 14a).[52,53] However, the defect discovered in *Fd$\bar{3}$m* structure cannot be built by using only these four polyhedra, three new types of polyhedra ($4^1 5^{10} 6^2$, $4^2 5^8 6^5$, and $4^1 5^{10} 6^4$) were employed, as shown in Figure 14b. All of them were discovered in Matzke's experiment on random foam structure.[54] The HRTEM image of the *Fd$\bar{3}$m* structure taken from [–110] direction is shown in Figure 14c with the simulated TEM image for a twin shown in a white rectangle. The structural model using the 5^{12} and $5^{12}6^4$
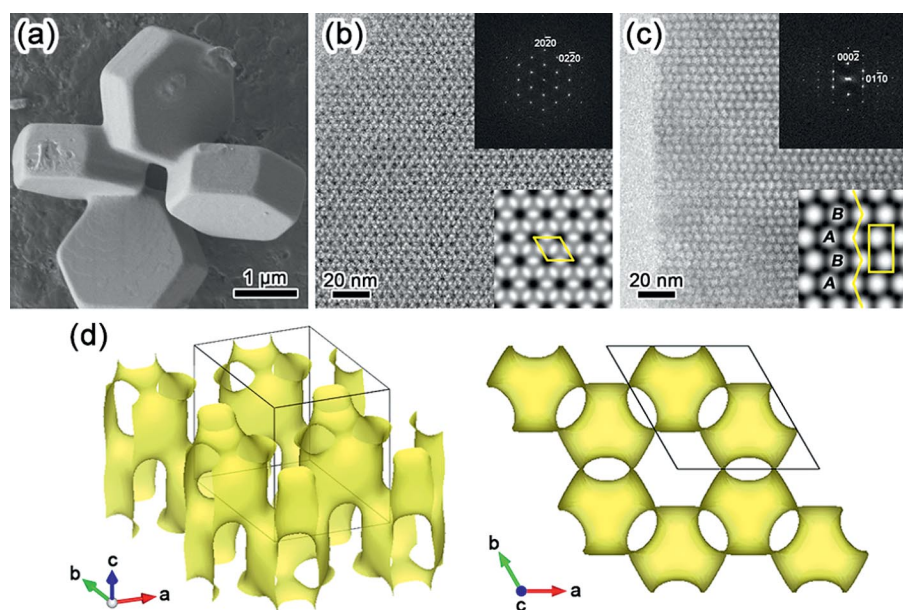
Figure 12. SEM images of the calcined SMC with hcp structure (a). HRTEM images taken at 200 kV by JEM-2100 from [0001] (b) and [2–1–10] axis (c) and the 3D reconstruction model of the electrostatic potential distribution of the calcined sample (d).[51]
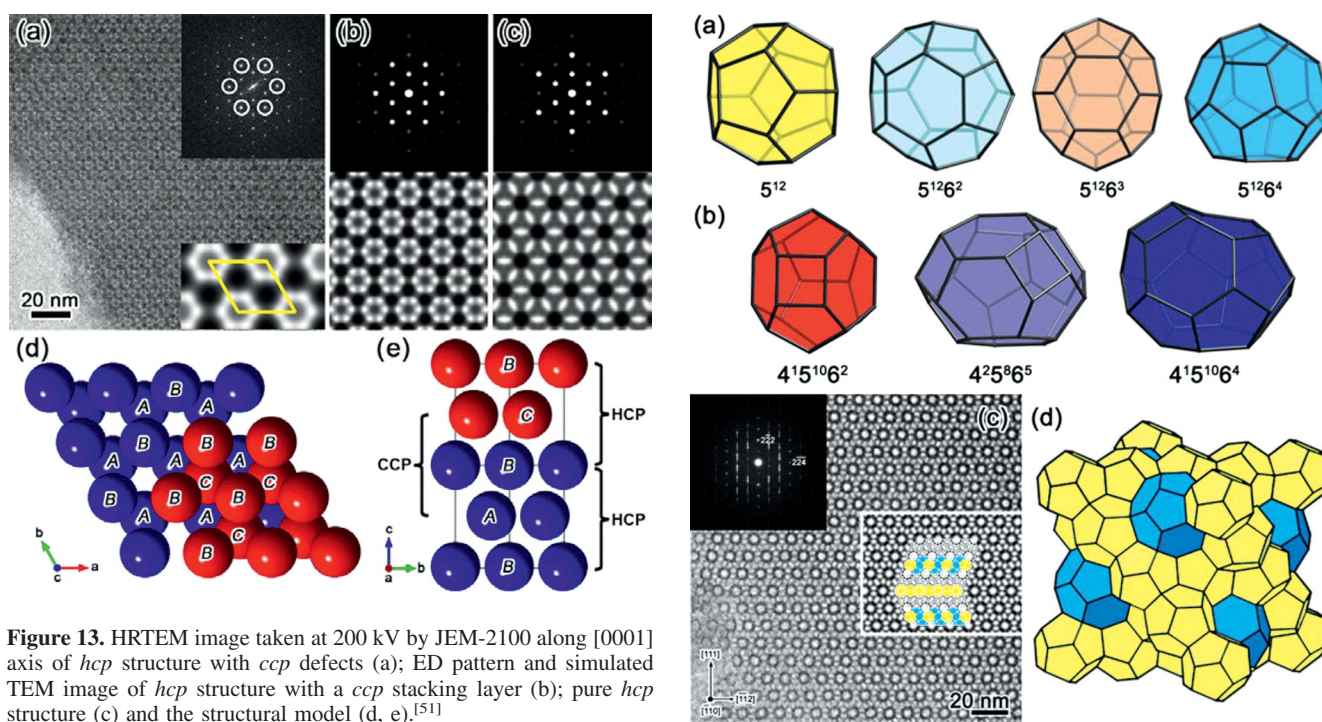

Figure 13. HRTEM image taken at 200 kV by JEM-2100 along [0001] axis of *hcp* structure with *ccp* defects (a); ED pattern and simulated TEM image of *hcp* structure with a *ccp* stacking layer (b); pure *hcp* structure (c) and the structural model (d, e).[51]

Figure 14. Schematic drawings of four types of Frank Kasper polyhedra (a), three types of polyhedral to construction the defect structure (b), the HRTEM image taken at 300 kV by JEM-3010 (c) and the structural description of the *tcp* mesostructures with *Fd3̄m* symmetry (d).[55,56]

are overlayed with the simulation and in Figure 14d, which agrees very well with the observed structure. Interstingly, in the *Fd3̄m* structure, several twinning, intergrowth and different defect structure were observed.

By control of the synthesis condition, the mesostructure changes from the spherical packing *ccp* (with *hcp* intergrowth) mixture structure to *Fd3̄m*. In the transition area, the intergrowth of these two structures was directly observed by HRTEM (Figure 15a). An epitaxial growth, in which the [–211] of the *ccp* structure corresponds to the [–101] of the

Fd3̄m structure sharing the (111) plane, suggesting that the *ccp* structure and the *Fd3̄m* structure has a 30° rotational relationship along the common [111] axis. The intergrowth can be described by introducing an intermediate layer between the *Fd3̄m* structure (polyhedra) and the *ccp* structure (spheres), as
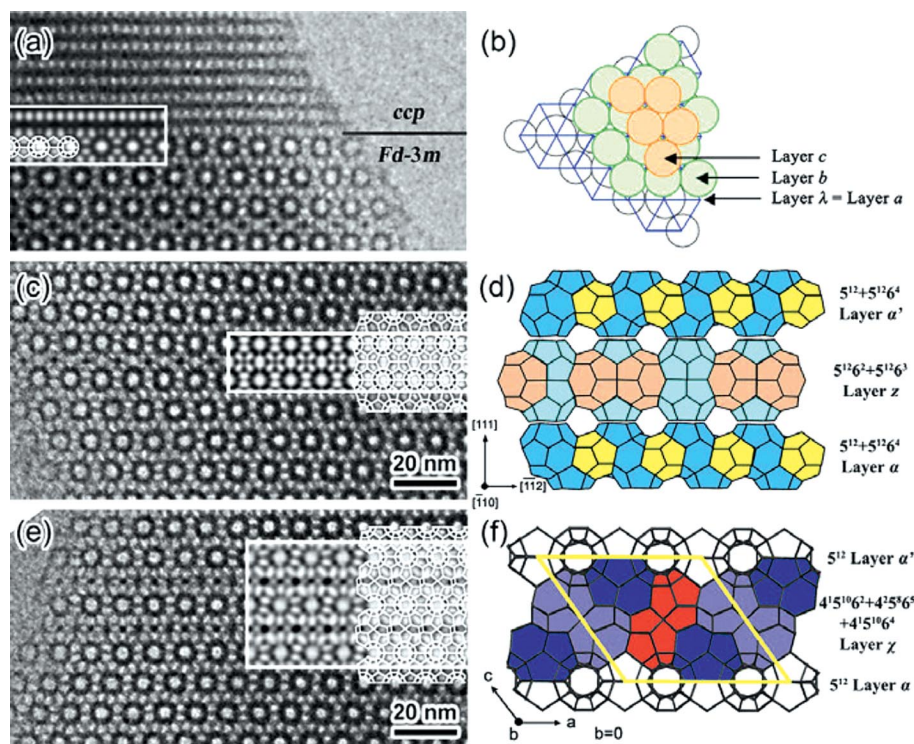
Figure 15. HRTEM images taken at 300 kV by JEM-3010 of the intergrowth of the *ccp* (*hcp*) and $Fd\bar{3}m$ structures taken from $[-110]_{Fd\bar{3}m}$ and $[-211]_{Fm\bar{3}m}$ axis with the simulated TEM images (a) and the schematic drawings of the boundary layer λ (b); the defect layer *z* from $[110]_{Fd\bar{3}m}$ (c) and schematic drawing (d); the defect layer χ from $[110]_{Fd\bar{3}m}$ (e) and the schematic model (f).[55,56]

shown in Figure 15b. The small spheres occupy the lattice point of the triangular net and the large spheres sit on the center of hexagon of the Kagomé net. The defect layer results in the base layer for the successive *ccp* structure and therefore the *ccp/hcp* layer can be placed on the top.[55]

Figure 15c shows the HRTEM images taken from the $[-110]_{cub}$ including a defect with hexagonal symmetry with space group *P6/mmm*. The defect layer *z* can be explained well by introducing two types of polyhedra $5^{12}6^3$ occupying an arrangement in the triangular net and $5^{12}6^2$ polyhedron located in the center of the triangle net. The schematic drawings of the layers and simulated TEM images of the defect are inserted in observed HRTEM images and shown in Figure 15d.[55,56]

Another type of defect has a monoclinic unit cell with space group *C2/m* and cannot be built by using only the four types of Frank-Kasper polyhedra, whereas three new polyhedra, $4^1 5^{10}6^2$, $4^2 5^8 6^5$, and $4^1 5^{10}6^4$, were employed (Figure 14b). As shown in the figure, simulated TEM images and the structure models have a good agreement with the observed HRTEM images (Figure 15e), which support the faithfulness of the structure model and brings the new possibility of constructing new cage-type structures by stacking the micelles with various type and size.[56]

(B-2-3) Toward Quasicrystalline State

Quasicrystalline softmatter has been reported in block-co-polymer systems as polymeric quasicrystals. Hence, we were excited to observe an SMC showing icosahedral morphology

and an ED patterns with ten-fold symmetry (Figure 16).[57,58] However, the material turned out not to be quasicrystalline but multiply-twined particles of *ccp* (space group $Fm\bar{3}m$) consisting of packing of tetrahedral domains sharing {111} surface, which is commonly observed in many face centered cubic crystals such as gold nanoparticles.
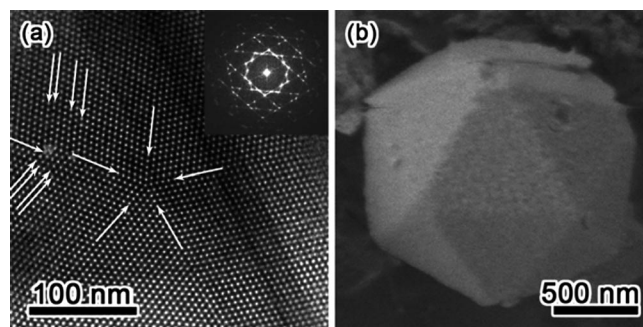

Figure 16. HRTEM images taken at 300 kV by JEM-3010 from the [110] axis of the multiply twinned *ccp* structure with decahedron shape (a) and the SEM image of the SMC with icosahedron morphology.[57,58]

Very recently, a new class of quasicrystal exhibiting 12-fold (dodecagonal) symmetry has been synthesized using SMC by the fine control of the reaction composition in the intermediate part of $Pm\bar{3}n$ and $P4_2/mnm$ structure regions. Three polyhedra packing structures, *Cmmm*, $Pm\bar{3}n$ and $P4_2/mnm$ that are represented as periodic tilings with squares and equilateral triangles, have been found to coexist, whereas the quasicrystallinity has

been verified by electron diffraction and quantitative phason strain analyses on TEM images obtained from the central region of the particle. A non-equilibrium growth process, wherein the competition between different micellar configurations takes place, has been proposed to play the central role in tuning the mesostructure (Figure 17).[59]
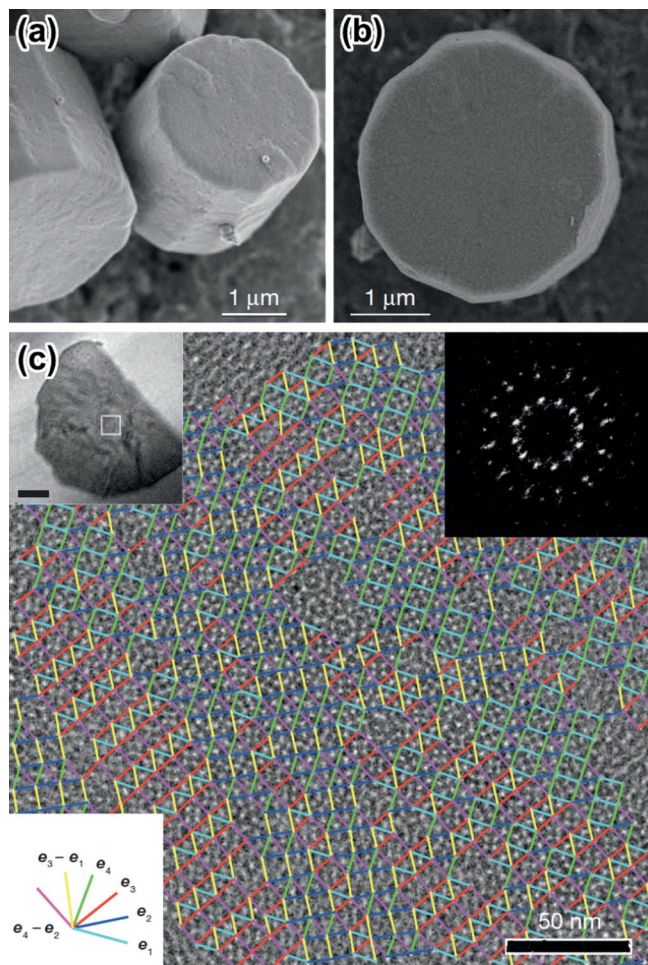

Figure 17. Mesoporous particles with dodecagonal morphology and associated electron microscopy. SEM images (a, b); the particles are dodecagonal prisms. Main panel (c), TEM image taken at 300 kV by JEM-3010 from the central part of the sample (as indicated in the top left inset; scale bar, 1 µm), where the tiling edges are superposed on the image. The colors of the edges correspond to the six unit vectors in physical space as shown in the bottom left inset. Top right inset, Fourier diffractogram of the main-panel image.[59]

(III) AFM and SEM

(A) Zeolites

For nanoporous framework materials such as zeolites, phosphates, and metal-organic framework materials it is very instructive to analyze the surface topology in nanoscopic detail in order to discern the structural signatures of crystal growth. In this regard a combination of high-resolution scanning electron microscopy (HRSEM) and AFM is particularly powerful. Both techniques can readily achieve the sub-nanometre resolu-

tion required to observe the structural features. AFM has the advantage that crystals can be observed in situ under growing or dissolving solution regimes. Further, the heights of surface features may be accurately determined which often leads to a direct assignment of the surface structure. The AFM can also be used to determine the energetics of dynamic processes occurring at the crystal surface and thereby go a long way to revealing the crystal growth mechanism. The drawback of AFM is that it is only plausible to observe a small number of crystals owing to the rate, at which micrographs can be collected and further the arrangement of the AFM tip sometimes precludes the clear imaging of complex surface features often observed, in particular, in highly intergrown crystals. HRSEM on the other hand overcomes these two restrictions permitting (i) the rapid observation of collections of crystals and (ii) the imaging of complex surface structures. The downside of HRSEM is the need to operate under vacuum, which means that crystals cannot be grown or dissolved in situ. As a consequence, the two techniques are highly complementary and form a powerful pair to probe crystal growth mechanism.

The power of AFM for in situ studies of crystal growth is illustrated in Figure 18, which shows the growth of a nanoporous zinc phosphate with the sodalite structure.[60,61] The images were recorded at ambient temperature every six minutes and show the progression of (111) surface topology. These images capture two modes of crystal growth (i) spiral growth at a screw dislocation and (ii) layer-by-layer growth. There are crucial differences between these two different growth modes that are very significant for general growth mechanisms in nanoporous framework materials. First, the height of the terraces is twice as high for the screw dislocation as the layer-by-layer growth. Second, the spiral growth presents a geometrical, triangular, growth form but the layer-by-layer growth presents an isotropic growth form. The reason for these observations is that the higher terrace has complete, through framework connectivity that, in turn, strongly delineates growth in different crystallographic directions and hence the threefold symmetry along the [111] direction is reflected in the threefold symmetry of the terrace. For the layer-by-layer growth the components of the terrace are not connected through the framework but
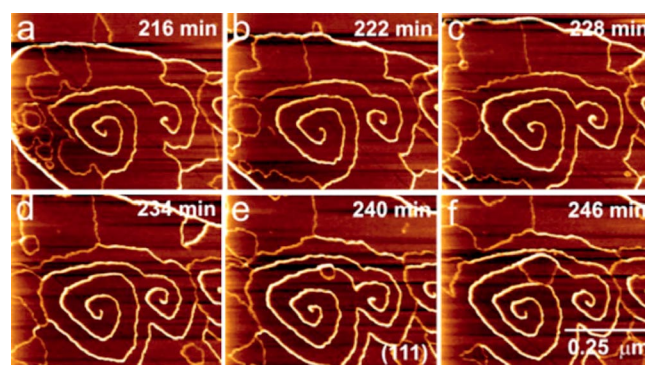

Figure 18. In situ AFM of the (111) surface of a nanoporous zinc phosphate with the sodalite structure. Each frame is separated temporally by six minutes and shows both spiral growth and layer-by-layer growth.[60]
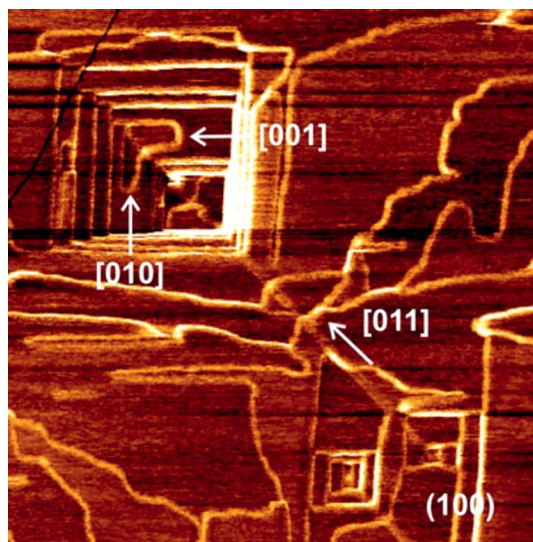
Figure 19. Defect structure on the (100) surface of nanoporous zinc phosphate with the sodalite structure.[60]

through more weakly interacting cations and water molecules. Hence, there is lack of preference for growth along a particular crystallographic direction. These rules can be brought to bear on the control of both terrace topology and ultimately overall crystal habit.

Figure 19 shows an AFM image of the (100) facet of the same zinc phosphate sodalite crystal and reveals a defect running along the [011] direction. At each side of the seam of the dislocation can be observed crystal terraces growing orthogonally to one another. This curious defect is a result of switching of the strict alternation of zinc and phosphorus in the framework. Such a defect is unlikely to be observable by TEM but is clearly revealed by the surface structure and the frozen signatures of the crystal growth process.

As the AFM tip is generally in contact with the crystal surface during the imaging there is always a possibility that the act of collection of data interferes with the chemical processes.

This can normally be mollified or eliminated either by working at very small tip/sample forces or, in the extreme, extrapolating data to zero force. However, in certain instances this tip sample interaction can be put to good use. Figure 20a shows an example of zeolite LTL whereby the tip has been continuously scanned across single data line that traverses a long, narrow terrace.[62] The sample is under a very mild alkaline solution that, on the timescale of the experiment, would hardly dissolve the crystal. However, the tip/sample interaction aids the dissolution and the terrace is cut through completely after 2330 s. Curiously, however, the terrace is not cut through in one continuous slice but in seven discrete steps each remaining stable for different lengths of time (Figure 20b). Each of these seven steps has a height of a few Ångstroms and each leaves a structure that consists of closed framework cages. That is, the metastable intermediate structures are all when the crystal achieves a new configuration whereby the new surface is always constructed from Q3 tetrahedral metal ions. Furthermore, as each dissolution step occurs the exothermic process imparts energy to the AFM tip, which results in a twisting of the cantilever. This can be monitored and the energy of each nanoscopic process determined (see Figure 20b).

When the surface features are more complicated then HRSEM is more appropriate than AFM. A case in point is the twinned crystal of zeolite LTA shown in Figure 21, where there is a steep angle between the two twinned (100) crystal faces. This is very awkward to access by AFM and the detailed structure along the twin line is completely inaccessible to AFM. The quality of the HRSEM images is sufficient to easily image the 1.2 nm high terraces on the individual facets of zeolite A and at the same time reveal the complex defect structure along the line of the twin.[63] It is to be noted that SEM has a large focus-depth, and that fine surface structural details in different height can be observed. Using a bias voltage applied to the specimen substrate, an electrostatic field is produced between the magnetic lens and substrate, which decelerates impact electrons to the specimen and extremely low landing energies can be used, which removes charging whilst maintaining a finely
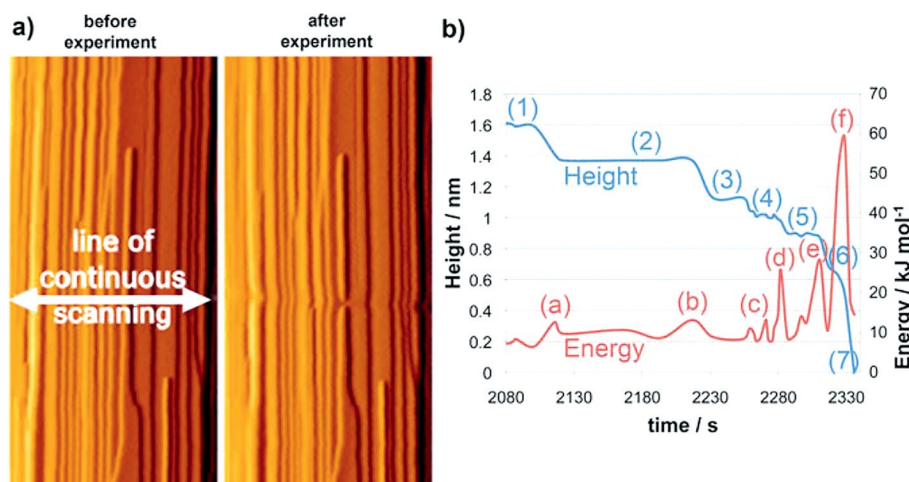

Figure 20. Tip-aided dissolution of zeolite LTL: (a) shows continuous terrace before experiment and terrace cut through after experiment and (b) shows the stepwise change in height of the terrace as it is cut through along with the associated force imparted to the AFM tip.[62]
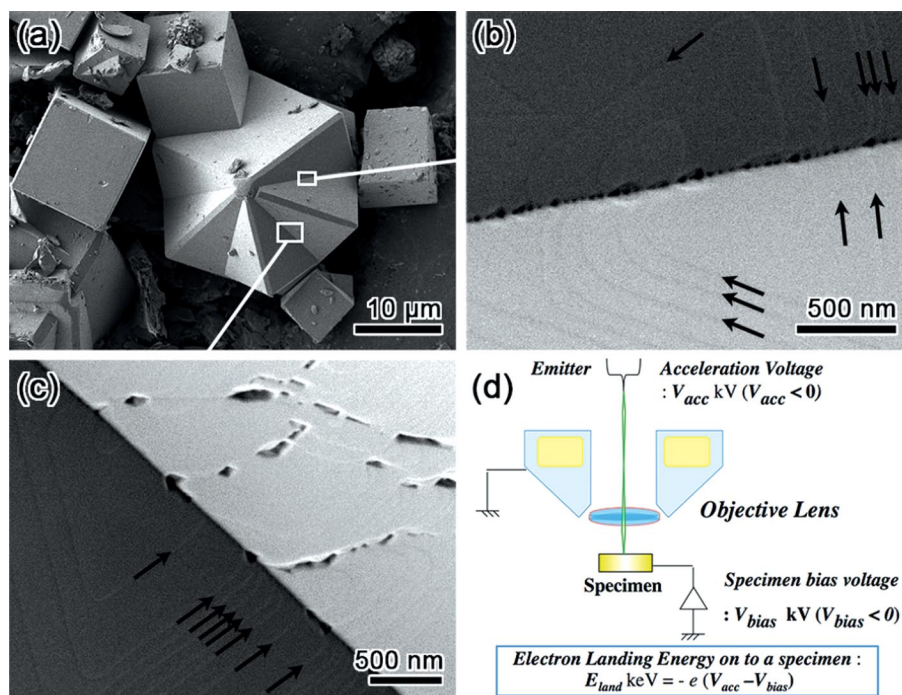
Figure 21. SEM image taken with JEOL JSM-7401F the landing energy of 1 keV after applying a specimen bias of –1.5 kV from a twinned crystal of zeolite LTA (a) and the magnified HRSEM images of the twinning part (b, c). Either side of the twin line 1.2 nm terraces can be observed on the two (100) surfaces. Along the line of the twin plane a string of defects are observed.[63] (d) Schematic drawing of the deceleration technique.

focused electron probe. A schematic drawing of the deceleration method is illustrated in Figure 21d.

(B) Mesoporous Silca, SBA-15

With the possibility to obtain improved resolution with the new generation LV-HRSEM more detailed information on mesoporous materials is achievable. In this section we will discuss how these new state-of-the-art microscopes provide information that hitherto has not been possible to obtain. We discuss and exemplify this by considering the well-known mesoporous silica material called SBA-15.[64] This material, synthesized in the wake of the seminal syntheses producing ordered mesoporous materials from *Inagaki* et al.[65] and *Beck* et al.[40] was in many ways a material with improved properties. Compared to the initial MCM-41 and FSM-16 materials it had not only larger pore diameter but also thicker silica walls giving it the improved stability that was desired in many applications. Initially SBA-15 was thought to be just a new "larger" version of MCM-41, as it had the same 2D structure as MCM-41 (plane group *p*6*mm*). It was however quickly realized that the porosity in SBA-15 was much more complex than was initially realized.[66,67] The frequently encountered image of SBA-15, depicting the structure as a simple rod-stacking of straight cylinders in an amorphous silica matrix, is an oversimplification that does not visualize the features that in many ways governs the properties of this material. We will give here two examples of how LV-HRSEM provides detailed information that allows us to better understand and describe the material properties [68].

Not long after the first synthesis of SBA-15 by *Zhao* et al. it was realized that the primary mesopores, arranged on a 2D hexagonal lattice, were accompanied by a set of smaller pores.[66,67] These pores are often referred to as micropores although the terminology is erroneous as the pore size of these complementary pores ranges from the micro- to the mesopore regime. A better terminology is intrawall pores and this term will be used in this paper. The existence of the intrawall pores was verified by a number of techniques, one of these being by replication experiments.[66,67] For instance when synthesizing Pt inside the porous framework of MCM-41 and of SBA-15 and subsequently removing the silica, the replica of the respective frameworks were obtained and found to be highly dissimilar [70].

Whereas the replica of MCM-41 produced elongated[71] and unconnected nanowires of Pt, the SBA-15 replica consisted of a 3D framework with nanowires connected via unordered "branches". The nanowires, for both materials, were formed by Pt crystallizing in the mesopores, but, for SBA-15, the intrawall pores also accommodated Pt and this created the connecting "branches". The intrawall pores are formed as the hydrophilic part of the structure directing amphiphile (i.e. the polyethyleneoxide chains) gets trapped within the silica framework and, during calcination, when the structure director is burnt off, this leaves an imprint in the silica wall.[66,67] The existence of intrawall pores is now thoroughly established from indirect techniques but the direct visualization of them has thus far been illusive. TEM images can, to a certain extent, demonstrate their existence[72] but the fact that the intrawall pores are unordered, and that TEM gives a 2D view of the 3D

object makes this technique less useful for visualizing these pores. SEM is therefore the method of choice and with the high resolution information provided by the LV-HRSEM it is now possible to directly image the intrawall pores. Figure 22 shows two SBA-15 materials, synthesized with two different structure directors, namely Pluronic P123 (Figure 22a) and Pluronic P104 (Figure 22b).[68] The particles are imaged from a direction more or less perpendicular to the *c* axis of the material and the primary mesopores are clearly depicted. The entrances of the intrawall pores can be seen as dark contrast patches within the mesopores, and some of these are marked with white arrows. It is clear that for both types of SBA-15, i.e. regardless of the synthesis being performed with P123 or P104, the material contain intrawall pores. It is also clear that the entrance size of the intrawall pores varies and that their occurrence is random.
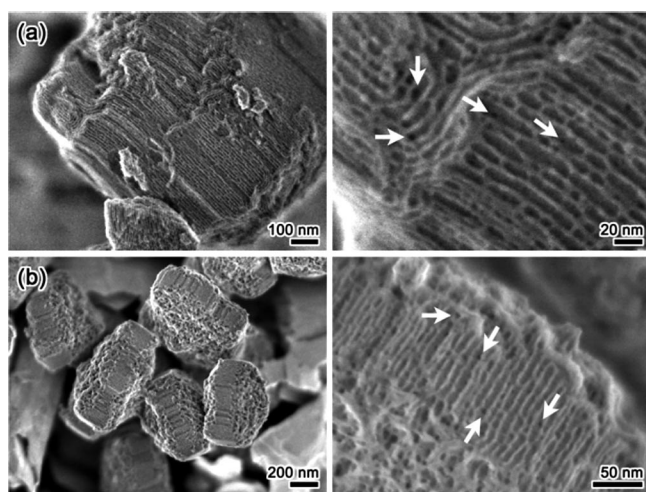

Figure 22. Side view SEM images of SBA-15 taken with JEOL JSM-7800F, the landing energy of 300 eV after applying a specimen bias of –5 kV, where the intrawall pores are shown, synthesized with P123 (a) and with P104 (b).[68]

We will now turn to another complication aspect of the porosity of SBA-15 but this time with reference to the main mesopores. As mentioned above, depicting the structure of SBA-15 as straight cylinders is inaccurate. Not only are the intrawall pores not included in this simplification but the main mesopores are in fact not straight cylinders. Rather the silica walls have a more corrugated appearance. In 2002 *Van der Voort* et al.[73] realized that the primary mesopores also contained some obstacles or "plugs". The existence of the plugs was revealed as the nitrogen sorption isotherms had an unusual tailing at the closure of the hysteresis. The nitrogen sorption isotherms of SBA-15 are expected to follow the type H1 hysteresis as defined by IUPAC, i.e. being defined by pores with cylindrical arrangement. However, the isotherms of SBA-15 showed evidence of tailing, which is typically the trait of pores with ink-bottle type behavior. Several other reports have discussed these plugs and it has been shown that the existence of plugs can have a more or less "severe" impact on the sorption behavior.[73] It has also been shown that by incorporating a polymer, that is preferentially located in the intrawall pores, a large portion of the porosity is inaccessible to the probing gas molecules.[74] This demonstrates that a substantial part of the porosity is only accessible via the intrawall pores. LV-HRSEM is an invaluable technique to directly monitor both the general corrugation in the mesopores and also its extreme case, that is, the existence of the plugs.[68] From images in Figure 23, it is obvious that the main mesopores are far from the simplified image of straight cylinder and are indeed highly corrugated. It is also obvious that in some cases, surprisingly often, the corrugation leads to a blockage of the main mesopore, i.e. a "plug". The SBA-15 materials in Figure 23 were synthesized under slightly varying conditions, which have an influence on how frequently these "plugs" occurs and this is clear from careful examination of the micrographs.
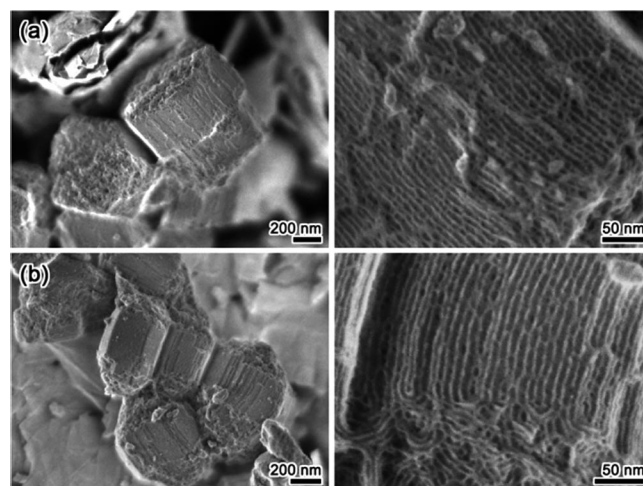

Figure 23. SEM images taken with JEOL JSM-7800F, the landing energy of 300 eV after applying a specimen bias of –5 kV from SBA-15 synthesized with P104 under different solvent conditions showing (a) several plugs and (b) less plugs.[68]

These properties, inherent to SBA-15 that can be directly detected only using LV-HRSEM, have a great impact on the properties of this frequently encountered mesoporous material. The possibility of direct visualization is naturally an enormous advantage. Images offer more detailed information providing both a better understanding for the material properties as well as giving data that facilitates the understanding of how these characteristic features are formed. It should however be noted that imaging of mesoporous material at this detailed level is limited to materials having very "clean" surfaces, and that the operator of the microscope needs a high level of experience.

(IV) Conclusions

The power of combinations of modern microscopy and diffraction tools, especially in the study of complex nanoporous architectures, was described. In the burgeoning area of mesoporous crystal architectures these methods have: revealed the detailed structure of quasicrystals with novel dodecagonal symmetry; successfully solved the structure through electron diffraction methods of a multitude of new phases; delineated structural transformations; helped to understand the complex

interconnectivity between hierarchical pore networks; revealed complex multiple twinning. All these structures have important lessons for the surfactant/polymer community as they represent the petrified fossilized structural forms of the more ephemeral soft mesostructures. The real power of the microscopy is to reveal the defects, intergrowths, disruptions non- and quasi-periodicity that is so difficult to extract from diffraction data alone. In the area of structure determination electron diffraction is the method of choice when the crystallites are themselves nanoscopic. This is often the case both in terms of achievable single crystals but also because crystals often intergrow. We have shown that automated methodology in this area has resulted in the successful determination of new zeolite structures and other porous materials. The real state-of-the-art is exemplified by studies using STEM-HAADF, which are able to identify individual metal atoms in a nanoporous framework structure. Ultimately, this will give the ability to pinpoint the precise nature of the active sites in a functional material, which are often isolated defects within the crystalline matrix. Finally, by combining EM tools with AFM it is possible to follow, in situ, crystal growth processes of nanoporous crystals from solutions and propose mechanisms based upon nanoscopic structural detail. With appropriate operation of the AFM it is also possible to extract the energetics associated with individual nanoscopic processes.

Acknowledgements

References

[1] M. Haider, H. Rose, S. Uhlemann, E. Schwan, B. Kabius, K. Urban, *Ultramicroscopy* **1998**, *75*, 53.

[2] A. Mayoral, R. Arenal, V. Gascon, C. Marquez-Alvarez, R. M. Blanco, I. Diaz, *ChemCatChem* **2013**, *5*, 903.

[3] A. Mayoral, R. M. Blanco, I. Diaz, *J. Mol. Catal. B* **2013**, *90*, 23.

[4] A. Mayoral, J. E. Readman, P. A. Anderson, *J. Phys. Chem. C* **2013**, *117*, 24485.

[5] A. Mayoral, T. Carey, P. A. Anderson, A. Lubk, I. Díaz, *Angew. Chem. Int. Ed.* **2011**, *50*, 11230.

[6] A. Mayoral, J. Coronas, C. Casado, C. Tellez, I. Díaz, *ChemCatChem* **2013**, *5*, 2595.

[7] D. L. Dorset, H. A. Hauptman, *Ultramicroscopy* **1976**, *1*, 195.

[8] A. Carlsson, T. Oku, J. O. Bovin, G. Karlsson, Y. Okamoto, N. Ohnishi, O. Terasaki, *Chem. Eur. J.* **1999**, *5*, 244.

[9] D. L. Dorset, C. J. Gilmore, *Z. Kristallogr.* **2011**, *226*, 447.

[10] P. Wagner, O. Terasaki, S. Ritsch, J. G. Nery, S. I. Zones, M. E. Davis, K. Hiraga, *J. Phys. Chem. B* **1999**, *103*, 8245.

[11] R. Vincent, P. Midgley, *Ultramicroscopy* **1994**, *53*, 271.

[12] P. Oleynikov, S. Hovmöller, X. D. Zou, *Ultramicroscopy* **2007**, *107*, 523.

[13] M. Gemmi, H. Klein, A. Rageau, P. Strobel, F. Le Cras, *Acta Crystallogr., Sect. B* **2010**, *66*, 60.

[14] U. Kolb, T. Gorelik, C. Kübel, M. T. Otten, D. Hubert, *Ultramicroscopy* **2007**, *107*, 507.

[15] E. Mugnaioli, U. Kolb, *Microporous Mesoporous Mater.* **2013**, *166*, 93.

[16] D. Zhang, P. Oleynikov, S. Hovmöller, X. D. Zou, *Z. Kristallogr.* **2010**, *225*, 94.

[17] T. Willhammar, J. L. Sun, W. Wan, P. Oleynikov, D. L. Zhang, X. D. Zou, M. Moliner, J. Gonzalez, C. Martínez, F. Rey, A. Corma, *Nat. Chem.* **2012**, *4*, 188.

[18] J. X. Jiang, J. L. Jorda, J. H. Yu, L. A. Baumes, E. Mugnaioli, M. J. Diaz-Cabanas, U. Kolb, A. Corma, *Science* **2011**, *333*, 1131.

[19] G. Bellussi, E. Montanari, E. Di Paola, R. Millini, A. Carati, C. Rizzo, W. O'Neil Parker, M. Gemmi, E. Mugnaioli, U. Kolb, S. Zanardi, *Angew. Chem. Int. Ed.* **2012**, *51*, 666.

[20] D. Denysenko, M. Grzywa, M. Tonigold, B. Streppel, I. Krkljus, M. Hirscher, E. Mugnaioli, U. Kolb, J. Hanss, D. Volkmer, *Chem. Eur. J.* **2010**, *17*, 1837.

[21] T. Ohsuna, Z. Liu, O. Terasaki, K. Hiraga, M. A. Camblor, *J. Phys. Chem. B* **2002**, *106*, 5673.

[22] F. Gramm, Ch. Baerlocher, L. B. McCusker, S. J. Warrender, P. A. Wright, B. Han, S. B. Hong, Z. Liu, T. Ohsuna, O. Terasaki, *Nature* **2006**, *444*, 79.

[23] Ch. Baerlocher, F. Gramm, L. Massueger, L. B. McCusker, Z. B. He, S. Hovmöller, X. D. Zou, *Science* **2007**, *315*, 1113.

[24] A. Mayoral, T. Carey, P. A. Anderson, I. Díaz, *Microporous Mesoporous Mater.* **2013**, *166*, 117.

[25] V. Alfredsson, O. Terasaki, J.-O. Bovin, *J. Solid State Chem.* **1990**, *84*, 171.

[26] O. Terasaki, T. Ohsuna, V. Alfredsson, J.-O. Bovin, D. Watanabe, K. Tsuno, *Ultramicroscopy* **1991**, *39*, 238.

[27] I. Díaz, E. Kokkoli, O. Terasaki, M. Tsapatsis, *Chem. Mater.* **2004**, *16*, 5226.

[28] T. Conradsson, M. S. Dadachov, X. D. Zou, *Microporous Mesoporous Mater.* **2000**, *41*, 183.

[29] Z. Liu, T. Ohsuna, O. Terasaki, M. A. Camblor, M. J. Diaz-Cabañas, K. Hiraga, *J. Am. Chem. Soc.* **2001**, *123*, 5370.

[30] B. Slater, C. R. A. Catlow, Z. Liu, T. Ohsuna, O. Terasaki, M. A. Camblor, *Angew. Chem. Int. Ed.* **2002**, *41*, 1235.

[31] B. Slater, T. Ohsuna, Z. Liu, O. Terasaki, *Faraday Discuss.* **2007**, *136*, 125.

[32] V. Alfredsson, T. Ohsuna, O. Terasaki, J.-O. Bovin, *Angew. Chem. Int. Ed. Engl.* **1993**, *32*, 1210.

[33] G. Oszlányi, A. Sütő, *Acta Crystallogr., Sect. A* **2004**, *60*, 134.

[34] G. Oszlányi, A. Sütő, *Acta Crystallogr., Sect. A* **2005**, *61*, 147.

[35] Y. Ma, P. Oleynikov, K. B. Yoon, O. Terasaki, in preparation.

[36] M. W. Anderson, O. Terasaki, T. Ohsuna, A. Philippou, S. P. MacKay, A. Ferreira, S. Lidin, *Nature* **1994**, *367*, 347.

[37] T. Ohsuna, O. Terasaki, D. Watanabe, M. W. Anderson, S. Lidin, *Microporous Titanosilicate ETS-10: Electron Microscopy Study, Zeolites And Related Materials: State of Art 1994*, in *Stud. Surf. Sci. Catal.*, *84* (Eds.: J. Weitkamp, H. G. Karge, H. Pfeifer W. Hoderich), Elsevier, **1994**, pp. 413.

[38] M. W. Anderson, O. Terasaki, T. Ohsuna, P. J. O'Malley, A. Philippou, S. P. Mackay, A. Ferreira, J. Rocha, S. Lidin, *Phil. Magn. B* **1995**, *71*, 813.

[39] C. T. Kresge, M. E. Leonowicz, W. J. Roth, J. C. Vartuli, J. S. Beck, *Nature* **1992**, *359*, 710.

[40] J. S. Beck, J. C. Vartuli, W. J. Roth, M. E. Leonowicz, C. T. Kresge, K. D. Schmitt, C. T. W. Chu, D. H. Olson, E. Sheppard, S. B. McCullen, J. B. Higgins, J. L. Schlenker, *J. Am. Chem. Soc.* **1994**, *116*, 10834.

[41] Q. Huo, Q. D. I. Margolese, G. D. Stucky, *Chem. Mater.* **1996**, *8*, 1147.

[42] A. Carlsson, M. Kaneda, Y. Sakamoto, O. Terasaki, R. Ryoo, H. Joo, *J. Electron Microsc.* **1999**, *48*, 795.

[43] Y. Sakamoto, M. Kaneda, O. Terasaki, D. Y. Zhao, J. M. Kim, G. Stucky, H. J. Shin, R. Ryoo, *Nature* **2000**, *408*, 449.

[44] K. Miyasaka, O. Terasaki, *Angew. Chem. Int. Ed.* **2010**, *49*, 9051.

[45] A. Jain, G. E. S. Toombes, L. M. Hall, S. Mahajan, C. B. Garcia, W. Probst, S. M. Gruner, U. Wiesner, *Angew. Chem. Int. Ed.* **2005**, *44*, 1226.

Special Issue

[46] Y. Han, D. Zhang, L. L. Chng, J. Sun, L. Zhao, X. Zou, J. Y. Ying, *Nat. Chem.* **2009**, *1*, 123.

[47] C. Gao, Y. Sakamoto, K. Sakamoto, O. Terasaki, S. Che, *Angew. Chem. Int. Ed.* **2006**, *45*, 4295.

[48] L. Han, K. Miyasaka, O. Terasaki, S. Che, *J. Am. Chem. Soc.* **2011**, *133*, 11524.

[49] A. E. Garcia-Bennett, C. Xiao, C. Zhou, T. Castle, K. Miyasaka, O. Terasaki, *Chem. Eur. J.* **2011**, *17*, 13510.

[50] L. Han, P. Xiong, J. Bai, S. Che, *J. Am. Chem. Soc.* **2011**, *133*, 6106.

[51] Y. Ma, L. Han, K. Miyasaka, O. Oleynikov, S. Che, O. Terasaki, *Chem. Mater.* **2013**, *25*, 2184.

[52] F. C. Frank, J. S. Kasper, *Acta Crystallogr.* **1958**, *11*, 184.

[53] F. C. Frank, J. S. Kasper, *Acta Crystallogr.* **1959**, *12*, 483.

[54] E. B. Matzke, *Am. J. Bot.* **1946**, *33*, 58.

[55] Y. Sakamoto, L. Han, S. Che, O. Terasaki, *Chem. Mater.* **2009**, *21*, 223.

[56] L. Han, Y. Sakamoto, S. Che, O. Terasaki, *Chem. Eur. J.* **2009**, *15*, 2818.

[57] K. Miyasaka, L. Han, S. Che, O. Terasaki, *Angew. Chem. Int. Ed.* **2006**, *45*, 6516.

[58] L. Han, Y. Sakamoto, O. Terasaki, Y. Li, S. Che, *J. Mater. Chem.* **2007**, *17*, 1216.

[59] C. Xiao, N. Fujita, K. Miyasaka, Y. Sakamoto, O. Terasaki, *Nature* **2012**, *487*, 349.

[60] M. A. Holden, P. Cubillas, M. P. Attfield, J. T. Gebbie, M. W. Anderson, *J. Am. Chem. Soc.* **2012**, *134*, 13066.

[61] M. A. Holden, P. Cubillas, M. W. Anderson, *Chem. Commun.* **2010**, *46*, 1047.

[62] R. Brent, P. Cubillas, S. M. Stevens, K. E. Jelfs, A. Umemura, J. T. Gebbie, B. Slater, O. Terasaki, M. A. Holden, M. W. Anderson, *J. Am. Chem. Soc.* **2010**, *132*, 13858.

[63] S. M. Stevens, PhD Thesis, Manchester, **2012**.

[64] D. Zhao, Q. Huo, J. Feng, B. F. Chmelka, G. D. Stucky, *J. Am. Chem. Soc.* **1998**, *120*, 6024.

[65] S. Inagaki, Y. Fukushima, K. Kuroda, *J. Chem. Soc. Chem. Commun.* **1993**, *8*, 680.

[66] R. Ryoo, C. H. Ko, M. Kruk, V. Antochshuk, M. Jaroniec, *J. Phys. Chem. B* **2000**, *104*, 11465.

[67] M. Kruk, M. Jaroniec, C. H. Ko, R. Ryoo, *Chem. Mater.* **2000**, *12*, 1968.

[68] T. Kjellman, S. Asahina, J. Schmitt, M. Impéror-Clerc, O. Terasaki, V. Alfredsson, *Chem. Mater.* **2013**, *25*, 4105.

[69] S. Jun, S. H. Joo, R. Ryoo, M. Kruk, M. Jaroniec, Z. Liu, T. Ohsuna, O. Terasaki, *J. Am. Chem. Soc.* **2000**, *122*, 10712.

[70] Z. Liu, O. Terasaki, T. Ohsuna, K. Hiraga, H. J. Shin, R. Ryoo, *ChemPhysChem* **2001**, *17*, 229.

[71] Z. Liu, Y. Sakamoto, T. Ohsuna, K. Hiraga, O. Terasaki, C. H. Ko, H. J. Shin, R. Ryoo, *Angew. Chem. Int. Ed.* **2000**, *39*, 3107.

[72] J. Fan, C. Yu, L. Wang, B. Tu, D. Zhao, Y. Sakamoto, O. Terasaki, *J. Am. Chem. Soc.* **2001**, *123*, 12113.

[73] P. Van Der Voort, P. I. Ravikovitch, K. P. De Jong, M. Benjelloun, E. Van Bavel, A. H. Janssen, A. V. Neimark, B. M. Weckhuysen, E. F. Vansant, *J. Phys. Chem. B* **2002**, *106*, 5873.

[74] N. V. Reichhardt, R. Guillet-Nicolas, M. Thommes, B. Klösgen, T. Nylander, F. Kleitz, V. Alfredsson, *Phys. Chem. Chem. Phys.* **2012**, *14*, 5651.

Special Issue